AGU PUBLICATIONS

JGR

Journal of Geophysical Research: Atmospheres

RESEARCH ARTICLE
10.1002/2016JD025422

Key Points:
- First observation and analysis of very long wave crests (450-500 km length) were carried out in NLC
- A ray-tracing analysis suggests a possible source of observed waves located in the upper tropospheric jet stream
- Gravity waves could propagate from the tropopause to the mesopause without reaching critical levels

Correspondence to:
P. Dalin,
pdalin@irf.se

Citation:
Dalin, P., et al. (2016), A case study of long gravity wave crests in noctilucent clouds and their origin in the upper tropospheric jet stream, *J. Geophys. Res. Atmos.*, *121*, doi:10.1002/2016JD025422.

Received 27 MAY 2016
Accepted 15 NOV 2016
Accepted article online 30 NOV 2016

A case study of long gravity wave crests in noctilucent clouds and their origin in the upper tropospheric jet stream

P. Dalin[1,2], N. Gavrilov[3], N. Pertsev[4], V. Perminov[4], A. Pogoreltsev[5], N. Shevchuk[3], A. Dubietis[6], P. Völger[1], M. Zalcik[7], A. Ling[8], S. Kulikov[9], A. Zadorozhny[10], G. Salakhutdinov[11], and I. Grigoryeva[11]

[1]Swedish Institute of Space Physics, Kiruna, Sweden, [2]Space Research Institute, RAS, Moscow, Russia, [3]Atmospheric Physics Department, Saint Petersburg State University, St. Petersburg, Russia, [4]A. M. Obukhov Institute of Atmospheric Physics, RAS, Moscow, Russia, [5]Meteorological Forecasts Department, Russian State Hydrometeorological University, St. Petersburg, Russia, [6]Department of Quantum Electronics, Vilnius University, Vilnius, Lithuania, [7]NLC CAN AM Network, Edmonton, Alberta, Canada, [8]Meteorological Service of Canada, Environment Canada, Edmonton, Alberta, Canada, [9]National Research Centre (NRC "Kurchatov Institute"), Moscow, Russia, [10]Division for Atmospheric Research, Novosibirsk State University, Novosibirsk, Russia, [11]Plasma Physics Department, National Research Nuclear University MEPhI (Moscow Engineering Physics Institute), Moscow, Russia

Abstract Atmospheric gravity waves with very long crests (of 450–500 km length) and short horizontal wavelengths of about 20 km were observed in noctilucent clouds and were studied in detail for the first time. The gravity waves were slowly moving in opposite direction to the background wind indicating their forced generation outside the mesopause region. A ray-tracing analysis using meteorological reanalysis and empirical atmospheric model data shows that a source of such peculiar gravity waves observed in noctilucent clouds was located near the tropopause and could be associated with the jet stream at altitudes 8–10 km. Two considered examples of very long wave crests confirm a significant role of the upper tropospheric jet stream as a source of gravity waves and reveal that these waves could propagate without critical levels to the mesopause in summertime.

1. Introduction

Night shining beautiful phenomena, noctilucent clouds (NLCs), are the highest clouds in the Earth's atmosphere, formed in the summer mesopause region at 80–90 km. NLCs are composed of water ice particles of several tens of nanometer in radius, which effectively scatter sunlight and are readily seen against the twilight sky. The clouds are seen from the end of May to September in the Northern Hemisphere and from the end of November to February in the Southern Hemisphere [*Bronshten and Grishin*, 1970; *Vasil'ev et al.*, 1987; *Gadsden and Schröder*, 1989]. When observed from space, these clouds are also called polar mesospheric clouds (PMCs).

Atmospheric gravity waves (GWs), permanently observed in NLC, have been extensively studied in recent decades. Ground-based studies have demonstrated that GWs, observed at the summer mesopause, have a broad spectrum of wavelengths ranging from small-scale (less than 10 km) [*Fritts et al.*, 1993; *Dalin et al.*, 2010] to large-scale size of 100–1000 km [*Witt*, 1962; *Rapp et al.*, 2002]. Based on a statistical study, *Pautet et al.* [2011] have demonstrated a strong anisotropy in propagation directions of GWs observed in NLC, with a majority of waves moving toward the NNE. Observations made from space have shown that gravity waves with horizontal wavelengths from at least 15 to 400 km are typical characteristics of PMC fields [*Chandran et al.*, 2009; *Taylor et al.*, 2011], and *Chandran et al.* [2010] have shown that there is a distinct anticorrelation of wave structures with PMC occurrence frequency and correlations with wave-induced temperature perturbations.

Larger-scale waves such as planetary waves, solar thermal tides, and lunar gravitational tides [*Kirkwood and Stebel*, 2003; *Dalin et al.*, 2011; *Fiedler et al.*, 2011; *Pertsev et al.*, 2015] influence the NLC evolution as well. Rare wave disturbances such as mesospheric fronts [*Dubietis et al.*, 2011; *Dalin et al.*, 2013] and voids [*Thurairajah et al.*, 2013] are also observed in NLC and PMC fields. *Baumgarten et al.* [2009] have comprehensively investigated a rogue gravity wave as observed in NLC, which produced strong temperature disturbances of 14–18 K.

Hines [1968] was probably the first who proposed the relationship between the tropospheric sources (fronts and jet streams) and major wave systems observed in NLC. *Yue et al.* [2014] have demonstrated that deep

convection in the troposphere may serve a source of concentric GW patterns in PMC fields. *Gerrard et al*. [2004] have found an influence of troposphere-generated gravity waves upon mesospheric clouds over Greenland. *Demissie et al*. [2014] have investigated 4 year climatology of GWs detected in NLC between 64 and 74°N. They found that the source of prominent wave structures observed in the NLC is likely to be located near the tropopause and is likely due to the coastal region of Norway along the latitude of 70°N. *Dalin et al*. [2015] have shown that the passage of an occluded tropospheric front can excite an isolated GW due to strong horizontal wind shears at about 5 km altitude, propagating upward to NLC heights. Atmospheric fronts and instabilities in the upper tropospheric jet stream are supposed to be among the tropospheric GW sources [e.g., *O'sullivan and Dunkerton*, 1995; *Uccellini and Koch*, 1987; *Zhang*, 2004]. Numerous studies were devoted to ray tracing of GWs observed at different altitudes in the atmosphere [*Bertin et al*., 1975]. *Marks and Eckermann* [1995] and *Eckermann and Marks* [1997] developed a 3-D nonhydrostatic model for GW ray tracing [see also *Eckermann and Marks*, 1996]. Ray tracing has been extensively used for interpreting ground-based and satellite observations and results of high-resolution numerical models [e.g., *Gerrard et al*., 2004; *Preusse et al*., 2009; *Sato et al*., 2012]. A review of sources and generation mechanisms of GWs can be found, for example, in *Plougonven and Zhang* [2014], *Sato et al*. [2009], and *Fritts and Alexander* [2003].

GWs are also regularly observed in airglow emission layers. When propagating through an airglow emission layer, a GW modulates its temperature and emission brightness. As a result, coherent wave-like structures are clearly detected in the OH, Na, O_2, and OI emission layers at the 80–100 km height interval [e.g., *Krassovski*, 1972; *Gavrilov and Shved*, 1982; *Taylor et al*., 1987; *Taylor and Hapgood*, 1988; *Swenson and Mende*, 1994; *Taylor et al*., 1995; *Vadas et al*., 2009]. *Paulino et al*. [2016] studied GW parameters in the lower thermosphere using observations of OI630 nm airglow images. *Gavrilov and Shved* [1982] statistically investigated medium- and large-scale internal GWs with periods of 0.5–5 h and wavelengths of 100–1700 km in the OI emission layer. *Swenson and Mende* [1994] observed monochromatic, multiple GWs as well as wave breaking followed by a very short-wavelength "rippled" structure in the OH airglow all-sky imagery. *Taylor et al*. [1987] observed the bright curved wave pattern of a short-period GW (21 min), and *Taylor and Hapgood* [1988] identified a thunderstorm as the most likely source of such a wave. *Taylor and Hapgood* [1990] studied OH emission small-scale mesospheric wave structure with horizontal wavelengths of 5–l5 km and lifetimes of less than 45 min (ripples) and found that these ripples are the result of short-lived velocity shears generated in situ by the combination of wind and wave motions. *Vadas et al*. [2009] investigated six medium-scale GWs with horizontal wavelengths of 60–160 km in the OH airglow layer. Based on the reverse and forward ray-tracing analysis to the tropopause and into the thermosphere, the authors identified the convective plumes, convective clusters, and convective regions which may have generated these waves, with deep convection being the most likely source of four of these waves. *Stockwell and Lowe* [2001] performed a statistical study of GWs seen in the OH emission layer (as observed from southwestern Ontario) and found the most common wave parameters being 45 m/s for horizontal phase speed, 25 km for horizontal wavelength, and 10 min for observed period, with the dominant direction of propagation toward the northeast. *Nakamura et al*. [1999] statistically investigated GWs as observed in the OH airglow emission in Japan and found typical wave parameters being in the range of 5–60 km for horizontal wavelengths, 5–30 min for observed periods, and 0–100 m/s for horizontal phase speeds. GWs observed in the OH layer with horizontal wavelengths of greater than 18 km were considered to be generated in the troposphere and propagated through the middle atmosphere, whereas small-scale waves ($<$17 km) were supposed to be mainly generated in situ in the mesosphere, with possible mixing with waves coming from the troposphere.

In the present paper, we analyze two cases of NLC displays exhibiting long crests of GWs with short horizontal wavelengths moving with very slow observed horizontal phase velocities. Using model simulations based on the reverse ray tracing as well as on analysis of assimilated meteorological data we study possible sources and generation mechanism of the observed GWs.

2. Available Data and Measurement Technique

Detailed observations of NLC displays exhibiting long crests of GWs were made on the nights of 6–7 July and 7–8 July 2014 with three synchronized automated digital cameras located at Krasnogorsk, Lobnya, and Obninsk (all the sites are located near Moscow, Russia, with average coordinates 55°39′N, 37°08′E). The NLC cameras take images of the twilight sky every minute during the night and belong to the network of

ground-based NLC cameras, dedicated to continuous monitoring of NLC activity in the Northern Hemisphere [*Dalin et al*., 2008; *Dubietis et al*., 2011]. The separation distances of several tens of kilometers between the stations allow the use of a triangulation technique for estimation of the NLC height and horizontal characteristic of GWs. The triangulation technique is based on a classical two-station triangulation method. The camera pairs Krasnogork-Obninsk and Krasnogorsk-Lobnya are utilized to estimate the NLC heights since some of NLC details have been obstructed by tropospheric clouds (in Obninsk) and by buildings (in Lobnya). The three cameras were synchronized to the local time (UTC + 4 h) with accuracy within 5 s. The detailed manual procedure was applied to the synchronous NLC images in order to estimate the same NLC points on a pixel-size base. It turned out that it is possible to estimate the same NLC points with accuracy of two pixels for the present cases.

The NLCs were determined at elevations angles of 3.3–5.3° and at azimuth angles of −8.2~+34.9° for the case of 7–8 July. In accordance to the error analysis of the NLC height given by *Dalin et al*. [2015], the precision of the height determination for this particular case of very low NLC elevation angles is in the range of 0.7–1.1 km, corresponding to the two-pixel uncertainty. Given the precision of synchronization and the two-pixel uncertainty of the NLC point identification, the total altitude uncertainty was estimated to be 0.9–1.3 km. This uncertainty is less than natural variability of the NLC heights, which was about 3 km for the present case. The total altitude uncertainty corresponds to the geolocation uncertainty of 5.0–7.6 km, which is small compared to the ray trace-modeled uncertainty and comparable to or less than the horizontal resolution of the European Centre for Medium-Range Weather Forecasts (ECMWF) model (7 × 14 km at a 60° latitude circle) discussed below. A full description of the NLC triangulation technique and its error analysis are given by *Dalin et al*. [2015].

3. Ray-Tracing Model Studies

In the present study, we suggest that long crests, observed in NLC, could be formed by GW propagating from the troposphere to the mesopause. In order to identify possible wave sources we have performed a reverse ray-tracing analysis of the observed GW using the numerical Acoustic-Gravity Wave-Wind (AGWWIND) model developed by *Bidlingmayer and Pogoreltsev* [1992] and by *Pogoreltsev and Pertsev* [1996]. The AGWWIND model is a nonhydrostatic model and similar to the model described by *Cole and Hickey* [1981] and *Hickey and Cole* [1988]. The model treats the vertical structure of an acoustic-gravity wave propagating through the atmosphere with realistic height profiles of the background wind and temperature as well as taking into account effects of turbulent and molecular thermal conductivity, viscosity, and GW dissipation due to radiative heat exchange, which are important in the middle atmosphere [e.g., *Marks and Eckermann*, 1995; *Fritts and Alexander*, 2003]. Vertical profiles of the background wind and temperature in the altitude range between 0 and 77 km are taken from the European Centre for Medium-Range Weather Forecasts (ECMWF) model [*Untch et al*., 2005], for which we use the TL1279/L137 model level data extracted on a 0.125° × 0.125° horizontal grid with a 6 h temporal resolution. Vertical profiles of the background wind and temperature between 78 and 100 km are taken from the Global Empirical Wind Model (GEWM) [*Portnyagin and Solovjova*, 2000] and from the NRLMSISE-00 model [*Picone et al*., 2002], respectively. The merging of the wind profiles between ECMWF and GEWM model in the height range of 77–78 km provides good agreement of the wind velocity components.

4. Results

4.1. Experimental Results

In general, very long crests of GWs were observed for about 1.5 h from 21:00 to 22:30 UT on 7 July 2014, and a sequence of NLC images (as well as NLC movie) can be downloaded at ftp://ftp.irf.se/outgoing/pdalin/NLC/NLC_MOVIE/Krasnogorsk_07_08_July_2014/. Figure 1 shows simultaneous images of the observed NLC field and long crests, taken from Krasnogorsk (Figure 1a), Lobnya (Figure 1b), and Obninsk (Figure 1c) at 21:27 UT on 7 July 2014. The red/white dots and corresponding numbers denote the positions of the analyzed wave crests. Four long crests were unambiguously identified from three sites making possible the triangulation technique to determine heights and horizontal parameters of the waves studied. Careful examination demonstrates that the wave crests are not continuous in space. It is obvious due to complex interplay between different kinds of GWs (GWs of different scales are very often observed in NLC) and due to turbulent

Figure 1. NLC images taken from (a) Krasnogorsk, (b) Lobnya, and (c) Obninsk at 21:27 UT on 7 July 2014. The red/white dots and corresponding numbers 1, 2, 3, and 4 mark the positions of the four analyzed crests of gravity waves. Nine point groups in Figure 1a are used to identify crests as long as possible and to measure their heights.

eddies, partly smearing out the structure of the long-wave crests. However, those interruptions are rather small compared with extension of the wave crests. Also, patches of the long-wave crests have similar width, synchronously traveling in the same direction (toward NNE) as sequence of the NLC images demonstrates. We believe that all these facts provide strong evidence of physically the same origin of very long crests of GWs, being observed at the mesopause at that time.

Due to a complex wave structure present in the NLC field, the crests of interest are recognizable to a greater extent in the sequence of NLC images for 6 min (between 21:27 and 21:33 UTC) taken with a 1 min time interval. Three images of this time interval are presented in Figure 2, which is a close-up of sequence of the NLC images taken at the Krasnogorsk station. The horizontal parameters of the wave crests were estimated in seven representative point groups shown in Figure 2, and the heights of the wave crests were estimated in nine representative point groups shown in Figure 1a. These parameters are as follows:

1. horizontal extent is between 457 and 492 km;
2. mean horizontal distance between the crests (wavelength) is 21.4 ± 3.5 km;
3. mean horizontal phase velocity relative to the ground is 11 ± 3 m/s;
4. mean observed period is 32.4 ± 10.3 min;
5. azimuth of horizontal phase speed is $11 \pm 5°$, counting from north to east; and
6. height of the crests ranges between 78.7 and 81.8 km, with mean height of 80.7 km.

The estimation of horizontal characteristics of the long-wave crests has been done statistically, that is, by means of tracing the seven point groups in a sequence of images (Figure 2), measuring their geographical coordinates and motion speed relative to the ground; then a mean value of each horizontal parameter and its error has been derived. The distance from crest 2 to 3 spans more than one wavelength since the crest groups 1–2 and 3–4 were separated by smeared crests due to a complex interplay between different waves,

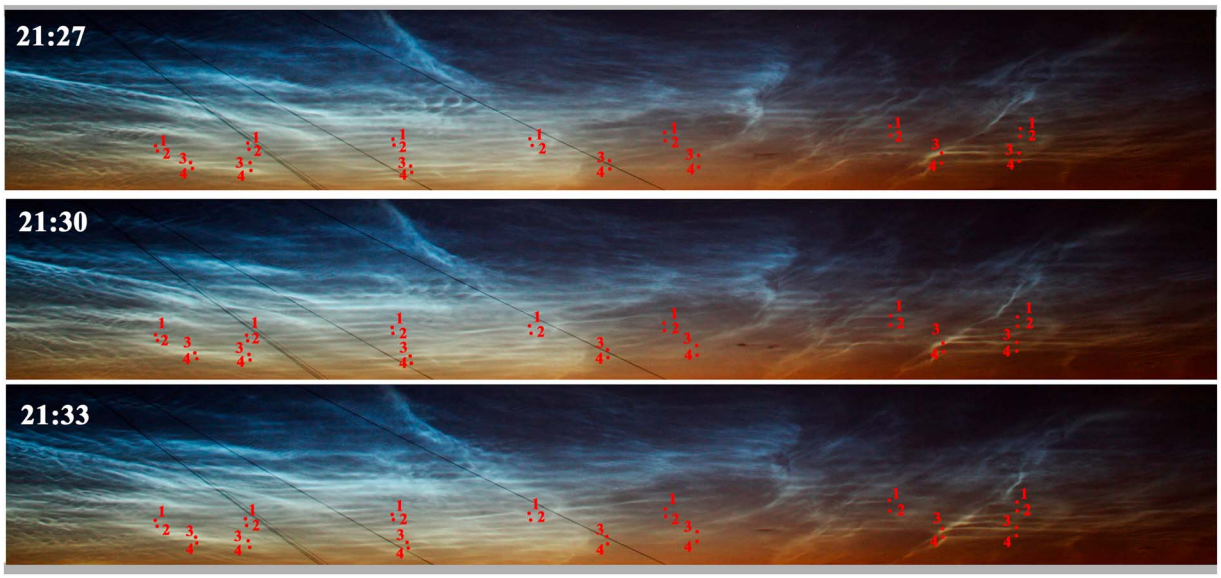

Figure 2. A close-up of a sequence of the NLC images taken at the Krasnogorsk station on the night of 7–8 July 2014. Three images at (top) 21:27, (middle) 21:30, and (bottom) 21:33 UT are shown. Seven point groups mark the position of the four analyzed crests of gravity waves evolved in time.

and it was impossible to unambiguously trace those crests which were presented between crests 2 and 3. Thus, the span between crests 2 and 3 has not been taken into account when calculating the horizontal wavelengths.

Such long horizontal extent of the GW crests is a remarkable feature of the present NLC display since similar long-wave crests with such short transverse wavelengths were never previously measured nor described in the field of NLC to the best of our knowledge. Therefore, we consider the observed wave crests as slowly moving approximately to the north and in opposite direction to the background wind (the overall NLC field, represented by small-scale as well as large transverse NLC structures, moved to the southwest). This fact indicates that the wave crests have not been formed at NLC heights, otherwise they would be moving together with the NLC field, but rather were generated at other altitudes. The heights of this generation could be lower as compared to the mean NLC height of 83 km as estimated from previous measurements [*Gadsden and Schröder*, 1989].

A temperature profile measured with the Sounding of the Atmosphere using Broadband Emission Radiometry (SABER) radiometer on board the Thermosphere-Ionosphere-Mesosphere Energetics and Dynamics satellite [*Russell et al.*, 1999], obtained at 21:25 UT on 7 July 2014 at coordinates 59.8°N, 28.6°E (Figure 3), for this particular time and space had several temperature minima between 78 and 82 km with vertical wavelength of ~3 km, which confirms the suitable conditions for the NLC existence at lower heights. Also, the temperature profile and the calculated the Brunt-Väisälä frequency (Figure 3, right) show clear wave oscillations between 71–76 km and 89–99 km with characteristic vertical wavelengths of 3–5 km, demonstrating possible propagation of respective GWs through the mesopause region. This issue will be addressed in section 5.

4.2. Results of Reverse Ray-Tracing Analysis

Assuming that the wave crests are produced by atmospheric GW, we made the reverse ray tracing by calculating GW group velocities with a 1 km height step. We use reference system with horizontal axis x in the propagation direction of GWs registered in noctilucent clouds, axis y in perpendicular direction, and vertical axis z. Using VKB approximation, *Bretherton* [1966] and *Jones* [1969] showed that GW group velocity can be represented as the sum of the mean wind and the group velocity in the windless atmosphere. In this approximation, GW trajectory $X(z)$, $Y(z)$ versus z can be described by equations

$$\frac{dX(z)}{dz} = \frac{C_x(z) + u_0(z)}{C_z(z)}; \qquad \frac{dY(z)}{dz} = \frac{v_0(z)}{C_z(z)}, \tag{1}$$

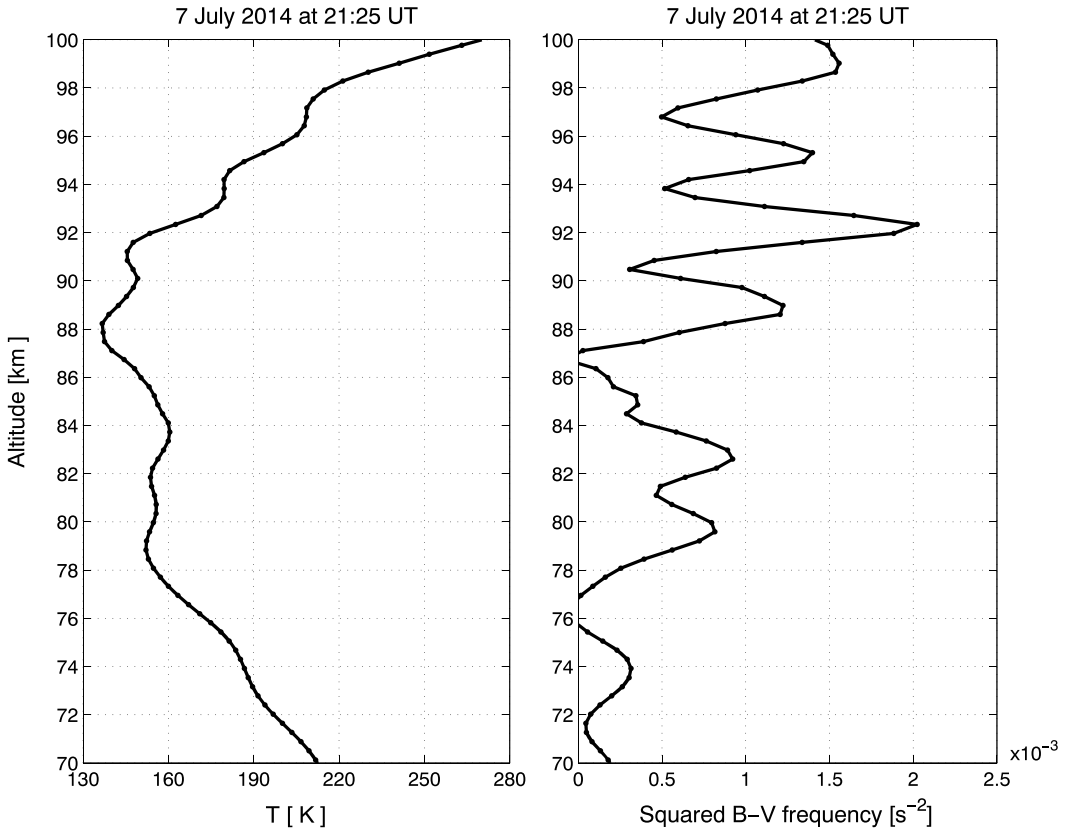

Figure 3. (left) TIMED/SABER kinetic temperature profile on 7 July 2014 at 21:25 UT at 59.8°N, 28.6°E. (right) The squared Brunt-Väisälä frequency is calculated using the temperature profile.

where $u_0(z)$ and $v_0(z)$ are the horizontal components of the background wind velocity along axes x and y, $C_x(z)$ is the horizontal GW group velocity relative to the mean wind, and $C_z(z)$ is the vertical GW group velocity. *Friedman* [1966] showed that the first equation in equation (1) is equivalent to $dX/dz = J_x/J_z$, where J_x and J_z are the components of the wave energy, which could be calculated by a GW numerical model. Using this approach, for solving the first equation in equation (1) we use the AGWWIND model (see section 3). The input parameters of the model (horizontal wavelength of the wave and its angular frequency) correspond to the observed wave crests seen in Figure 1. A combination of $X(z)$, $Y(z)$, and z yields an effective 3-D trajectory of the observed GW packet. Due to large values of $v_0(z)$ and small values of $C_z(z)$ the transverse displacements turned out to be large ($Y(z)$~780 km at $z = 10$ km). Therefore, a supposed region of the wave generation occurred to be significantly eastward of the mean meridian of the NLC crests (see Figure 5).

Realistic profiles of the background temperature and wind for solving equation (1) are taken from the ECMWF, GEWM, and NRLMSISE-00 models (see section 3). We calculated the *oblique* (not vertical) temperature and wind profiles along the wave trajectory, and their projections on vertical planes x-z and y-z are shown in Figure 4a. The results of the calculations are the backward trajectory projections $X(z)$ and $Y(z)$, propagation time, and vertical structure of the wave.

During an upward propagation of the GW originating from tropospheric sources, a partial reflection of wave energy in areas with fast increasing wave dissipation in the thermosphere may occur [*Yanowitch*, 1967]. Downward propagating reflected waves may interfere with the upward propagating original GW, increasing errors in the reverse ray tracing of the wave energy. Therefore, we developed a method of separation of the upward propagating GWs from the downward wave modes in the WKB solutions of the AGWWIND model, which provides more precise reverse ray tracing of the wave energy.

The AGWWIND model does not take into account changes of horizontal GW wave number k directed along axis x, which can vary due to horizontal gradients of background fields [e.g., *Andrews et al.*, 1987]. Using

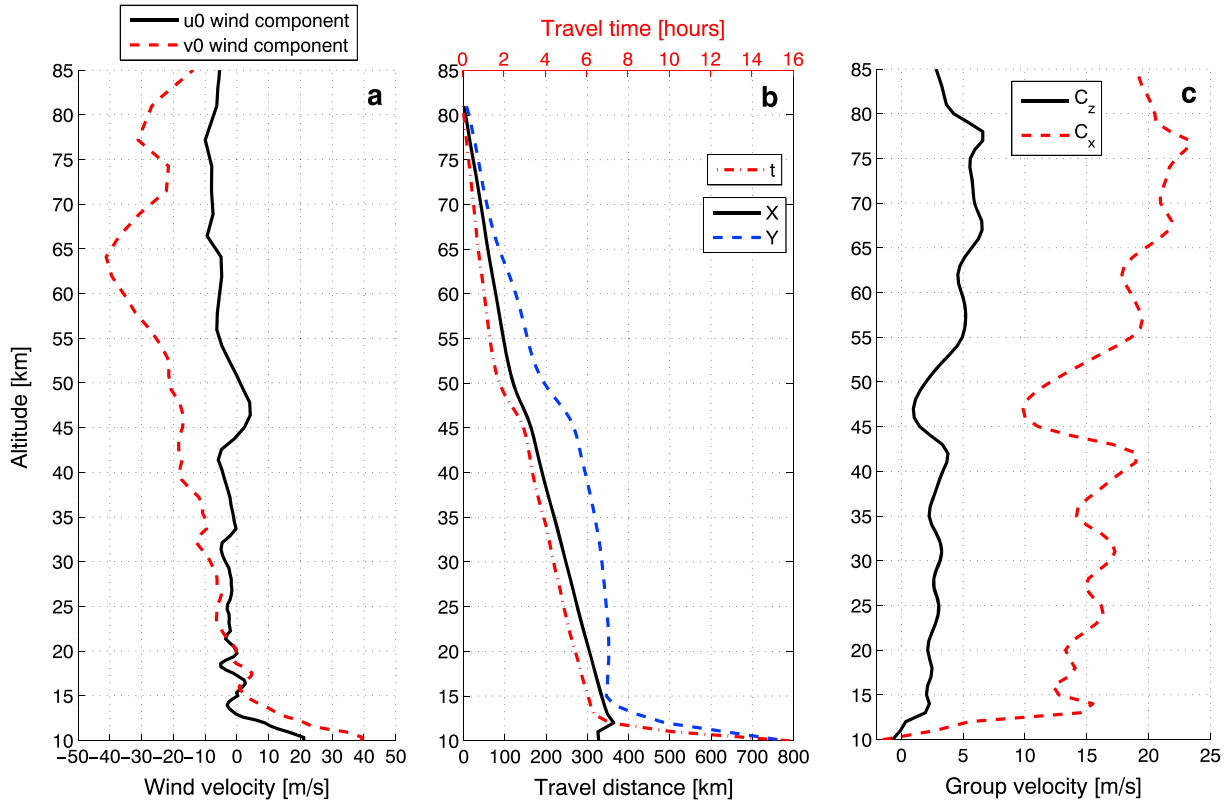

Figure 4. (a) Profiles of the wind velocity parallel (u_0) and perpendicular (v_0) to the wave vector. The profiles are calculated from the ECMWF and GEWM models at 12:00 UT on 7 July 2014. (b) Reverse ray-tracing analysis showing the wave-traveled distance parallel (*x* axis) and perpendicular (*y* axis) to the horizontal wave vector and its traveled time (*t*). The *x* axis is directed to 11° counting from the north to east, and the *y* axis is directed at the right angle to the *x* axis. (c) Vertical (C_z) and horizontal (C_x) group velocities of the GW.

equations (4A.3) and (4A.9a) from *Andrews et al.* [1987] we can estimate possible relative deviation of wave trajectory $|\delta X/X(z)| \sim |\delta k/k| \sim |\partial u_0/\partial x|t$, where $|\partial u_0/\partial x|$ is the average horizontal gradient of the mean wind along the middle part of the wave trajectory, t is the time interval for GW to reach NLC region ($z \approx 80$ km) from altitude z. Using the ECMWF, GEWM, and NRLMSISE-00 models we obtained the value $|\partial u_0/\partial x| \sim 1.2 \times 10^{-6}\,s^{-1}$ for $z \sim 12$ km with the standard deviation of $4.3 \times 10^{-6}\,s^{-1}$ of the gradient values at higher altitudes. These values in combination with travel times t of the GW propagation from Figure 4b lead to the estimate $|X/X(z)| \sim 0.03$ at $z \sim 12$ km with possible average deviations $|\delta X/X(z)| \sim 0.05$ at higher altitudes. These values are small, suggesting that assumption of constant k cannot significantly influence our calculations of the GW trajectory. To check if a possible change in the orientation of the wavefront could take place, we have applied the same procedure for left and right ends of the wavefront. The relative deviations of the wave trajectory $|\delta k/k|$ are 0.04 and 0.03 at the right and left ends, respectively. These values are small, suggesting that there was no large change in the orientation of the wavefront in the space-time domain considered.

Figure 4b illustrates the horizontal traveled distances of the wave packet along the wave vector $X(z)$, its transverse displacement $Y(z)$, and its travel time. Figure 4c shows the respective vertical and horizontal group velocity components. Above 12 km, all the parameters change smoothly with altitude, indicating the absence of either levels with strong wave dissipation or critical levels, suggesting free upward propagation of the observed GW from 12 to at least 80 km. However, there appear sharp changes in the considered parameters at 10 km, and the profiles beneath this altitude are unrealistic. This is due to the presence of a strong jet stream with speeds up to 40–45 m/s at the given space domain of the tropopause, creating critical levels for the considered slowly moving GW with phase velocities of about 11 m/s. These critical levels block the propagation of such GW, propagating from the troposphere to the stratosphere in directions toward the NNE-SSE sector.

4.3. Analyses of the ECMWF Wind and Temperature Fields

As demonstrated in Figure 4b, the traveled time is estimated to be 7.1 h and the traveled distance is 364 km for the wave packet travelling downward from 80 km to 12 km. Since the very long wave crests were observed from 21:00 to 22:30 UT on 7 July 2014, according to the reverse ray tracing, the GW responsible for the crest formation may be generated around the tropopause at times between 13:30 and 16:00 UT on 7 July 2014. Since we use the ECMWF model data with a temporal resolution of 6 h there are two nearby times at 12:00 UT and 18:00 UT to the time interval of the wave generation. For these times we analyze a mesoscale structure of the temperature and wind fields in the vicinity of a possible wave generation region as well as estimate the intensity of the ageostrophic sources of GW around the tropopause at 10–12 km.

4.3.1. Two-Dimensional Fourier Filtering Analysis of the Temperature Field

For studies of mesoscale wave processes we apply a Fourier filtering procedure to the ECMWF temperature field, based on 2-D spatial filtering in the wave number domain along latitude and longitude. We choose the Butterworth digital band-pass filter with a passband corresponding to about 14–1000 km along the parallel of latitude and 28–140 km along the meridian since the ECMWF model has a respective spatial resolution of about 7×14 km at a 60° latitude circle.

The top plot of Figure 5 demonstrates the result of the 2-D filtering analysis at 12:00 UT on 7 July 2014 at 12.6 km altitude. We have selected to show this altitude since the greatest amplitudes of temperature wave disturbances are observed at 12.6 km; also, this altitude is rather close to the tropopause region at 10 km. One can see two positive crests and one negative wave trough which coincide well (by orientation and extension) with the calculated position (B) of the NLC crests using the reverse ray-tracing analysis. The horizontal shear in the winds is located at the very beginning of the wave generation near the tropopause, which determines the original orientation of the wavefront but not changing its orientation during the propagation time. At the same time, the horizontal wavelength of temperature wave perturbations is about 2–3 times greater than the observed horizontal wavelength of NLC crests of about 20 km. This is because the long crests are being oriented approximately along the parallel of latitude, and model input data from ECMWF can only resolve wavelengths of 28 km or more. This is a consequence of limited resolution of ECMWF analysis data of 0.125°, corresponding to the sampling rate of 14 km along the meridian. On the other hand, both at around 10 km and in the NLC layer a spectrum of gravity waves of several wavelengths may exist. If two waves of equal energy but of different horizontal wavelengths perturb a noctilucent cloud layer, the wave of lesser wavelength would have been seen better because of larger vertical tilt of the streamlines, when regarding geometric curvature of an NLC layer as the most probable reason of visible wavelike structures [*Witt*, 1962]. That is why the detected wavelengths in troposphere and mesosphere may differ. Note that the position B of the crests is significantly eastward of the original position A of the crests observed in NLC, which is due to the above mentioned large transverse displacement of the wave packet. Similar patterns of temperature wave disturbances (of somewhat less amplitudes) have been retrieved at 18:00 UT (not shown).

Figure 5 shows the error estimations in the position of the calculated position (B) of the NLC crests. This error bar includes uncertainties in the temperature and wind profiles for the ECMWF model [*Bonavita*, 2011; *Cardinali et al*., 2014] and for the GEWM model [*Portnyagin and Solovjova*, 2000]. In general, the relative errors in the temperature are less than 5%, and the relative errors in the wind velocity vary from 50% in the lower thermosphere and upper mesosphere down to 15% in the troposphere, resulting in about a 20% uncertainty in the final position of the NLC wave crests at about 10 km. The uncertainties of the wave trajectory due to dissipative processes (turbulent, molecular, and radiative damping) are negligibly small compared to the uncertainties in the wind velocity profile; we have checked this issue by removing and adding dissipative processes in the model runs.

4.3.2. Nonlinear Ageostrophic Wave Sources

One of the mechanisms for the GW generation can be continuous interruptions of the geostrophic equilibrium of wind and geopotential fields and their permanent adjustments to this equilibrium. *Medvedev and Gavrilov* [1995] have demonstrated that the main strength (G_0) of the nonlinear generation of GW due to the geostrophic adjustment can be described by the following expression (their equation (18)):

$$G_0 = \left(\frac{\partial u}{\partial x}\right)^2 + 2\frac{\partial u}{\partial y}\frac{\partial v}{\partial x} + \left(\frac{\partial v}{\partial y}\right)^2, \quad (2)$$

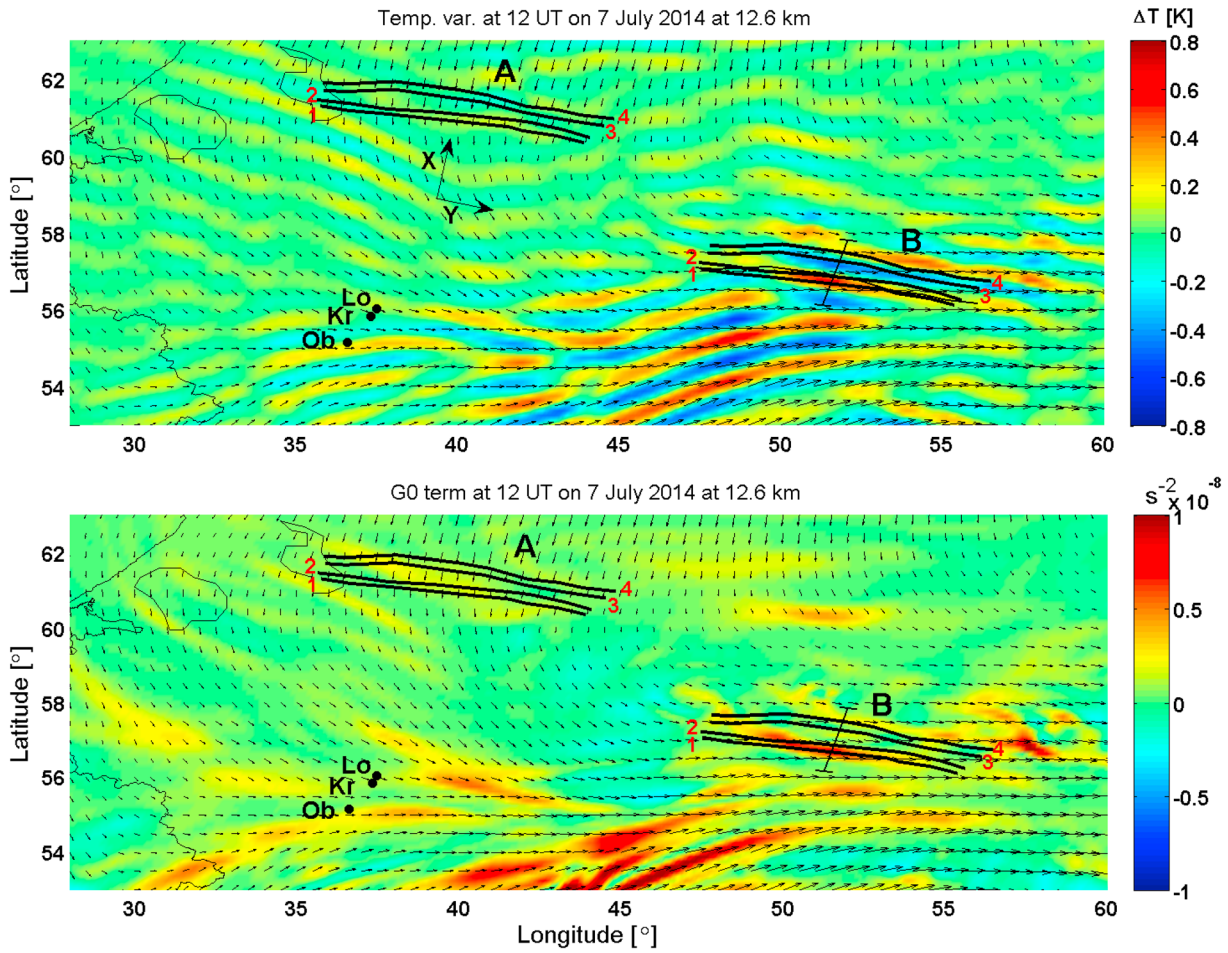

Figure 5. (top) Temperature wave disturbances at 12.6 km estimated from Fourier filtering analysis using the ECMWF data at 12:00 UT on 7 July 2014. The *x* and *y* axes show the reference system used in the paper, in which the *x* axis is oriented in the direction and parallel to the wave vector and the *y* axis is at the right angle to the wave vector of the GW. (bottom) Spatial distribution of the nonlinear wave source G_0 using equation (2). The black lines and corresponding numbers 1, 2, 3, and 4 at the position A show the long-wave crests observed in NLC. The black lines at the position B indicate their calculated backward position at $h = 12.6$ km using the reverse ray tracing. The uncertainty of the wave position is shown by the black error bar in the middle of the position B, based on uncertainties in the background wind and temperature profiles (see the text). The black arrows show the ECMWF wind field. The Lo, Kr and Ob symbols indicate the observation sites Lobnya, Krasnogorsk, and Obninsk, respectively.

where *u* and *v* are the zonal and meridional wind components along *x* and *y* axes, respectively. The bottom plot of Figure 5 shows the spatial distribution of G_0 calculated based on input data from the ECMWF model at 12:00 UT on 7 July 2014.

One can see strong bands of positive and negative G_0 values in the region of supposed generation of the long crests (position B). These bands are generally elongated in the mean flow directions and are approximately parallel to the wave crest positions B in the bottom plot of Figure 5. If we compare the top and bottom plots of Figure 5, one can see similar features in the both plots, namely, long crests in the temperature and in the wave source field at the position B, where the long NLC wave crests were generated. Note that we have used different input data as well as different analysis techniques to obtain the results shown in the top and bottom plots of Figure 5: the filtering procedure of the temperature field was applied to the former, whereas rigorous analytical solution for the wind field was applied to the latter. But the obtained wave disturbances at the position B look similar. It is important to note that disturbances in both the temperature field and the G_0 source are oriented along the jet stream propagating to the northeast in the middle bottom part of Figure 5 (top and bottom plots) and then rotating to the east and to the southeast direction in the bottom right corner of the figure; the rotation of the wave disturbances follows the rotation of the jet stream.

4.4. A Second Case of Long-Wave Crests Seen in NLC on the Night of 6–7 July 2014

Now we consider a second case of long-wave crests seen in NLC on the previous night of 6–7 July 2014. The wave crests were not as long as those on 7–8 July. The parameters of the gravity wave of the second case were rather similar to those obtained for the first case (excepting the horizontal extent of the wave crests):

1. horizontal extents of wave crests are between 151 and 156 km;
2. mean horizontal wavelength is 18 ± 3 km;
3. mean horizontal phase velocity is 17 ± 3 m/s;
4. mean observed period is 18 ± 4 min; and
5. azimuth of horizontal phase velocity motion is $20 \pm 4°$, counting from north to east.

The top part of Figure 6 illustrates the long-wave crests (marked by the red dots) as observed from Krasnogorsk at 21:00 UT on 6 July 2014. These crests were also observed from Lobnya and Obninsk, but we do not show corresponding images since they look very similar. As stated above, the horizontal extents of these crests were about 150 km only; however, even such a "small" horizontal extent is worth studying since such long-wave crests with a small wavelength of 18 km were not studied in detail in noctilucent clouds. In fact, one can see discontinuous parts of the long crests in the left part of the image, but a complex interference picture with other gravity waves does not allow us to unambiguously retrieve the long-wave crests from the left part of the image; thus, we further analyze the long crests clearly seen in the right part of the image.

As in the first analyzed case, the long-wave crests were slowly moving toward the NNE against the main flow of NLC, suggesting the location of their source beneath the mesopause region. The same reverse ray-tracing analysis was applied to the long crests in order to identify their possible source in the lower atmosphere. We do not show vertical profiles of the reverse ray tracing since they look rather similar to those shown in Figure 4, but we demonstrate the most important findings regarding the source of the wave crests, which are shown in the two bottom plots of Figure 6. One can see extended wave disturbances in the temperature field (bottom left plot) as well in the G_0 source (bottom right plot) in the position B of the wave generation around the tropopause at 10 km. We have selected this particular height to demonstrate the strongest oscillations in the temperature and in the G_0 source around the tropopause, but the actual height of the wave generation is slightly lower since the jet stream of 35–40 m/s at 8–9 km is also present in this case, where ageostrophic wave source G_0 is generated [e.g., *Gavrilov et al*., 1999, 2001]. This jet stream also creates critical levels and prevents propagation of GW with small horizontal phase velocities from the lower tropospheric wave sources to the stratosphere. The bottom plots of Figure 6 are shown for the ECMWF input data at 18:00 UT on 6 July 2014, which is the closest time for the generation of the gravity wave around the tropopause according to the reverse ray-tracing analysis for the second case. Note that the greatest portion of extended wave disturbances seen in the temperature and in the G_0 source is located northwest of the long generated crests (at the position B) but, as stated above, the left (northwest) part of the observed long crests in NLC is impossible to unambiguously retrieve due to a complex interplay with other GWs. However, some signatures of the long crests can be traced on the northwest side of the images, suggesting that longer-wave crests could be readily generated by the extended wave disturbances northwest of the position B as shown in the bottom plots of Figure 6. Thus, the second case also shows good agreement between the generated long-wave crests and extended wave disturbances at 10 km due to the upper tropospheric jet stream.

5. Discussion

We do observe similar long crests of gravity waves in NLC from time to time at many sites using imagery of our global NLC network [see, for example, *Dubietis et al*., 2010, Figure 1]. However, such long crests (~500 km) having a very short wavelength of about 20 km have not been described in the literature on NLC studies so far. That is why we consider long-wave crests studied in detail in the present paper to be unique.

Pautet et al. [2011] have statistically found that a majority of GWs seen in NLC move toward the NNE. The authors have noticed that "This anisotropy and the difference in the phase speed distribution cannot be explained by the filtering due to the background wind field but more probably by the position of the gravity wave sources, located to the south of the observation site." The present study partly confirms this

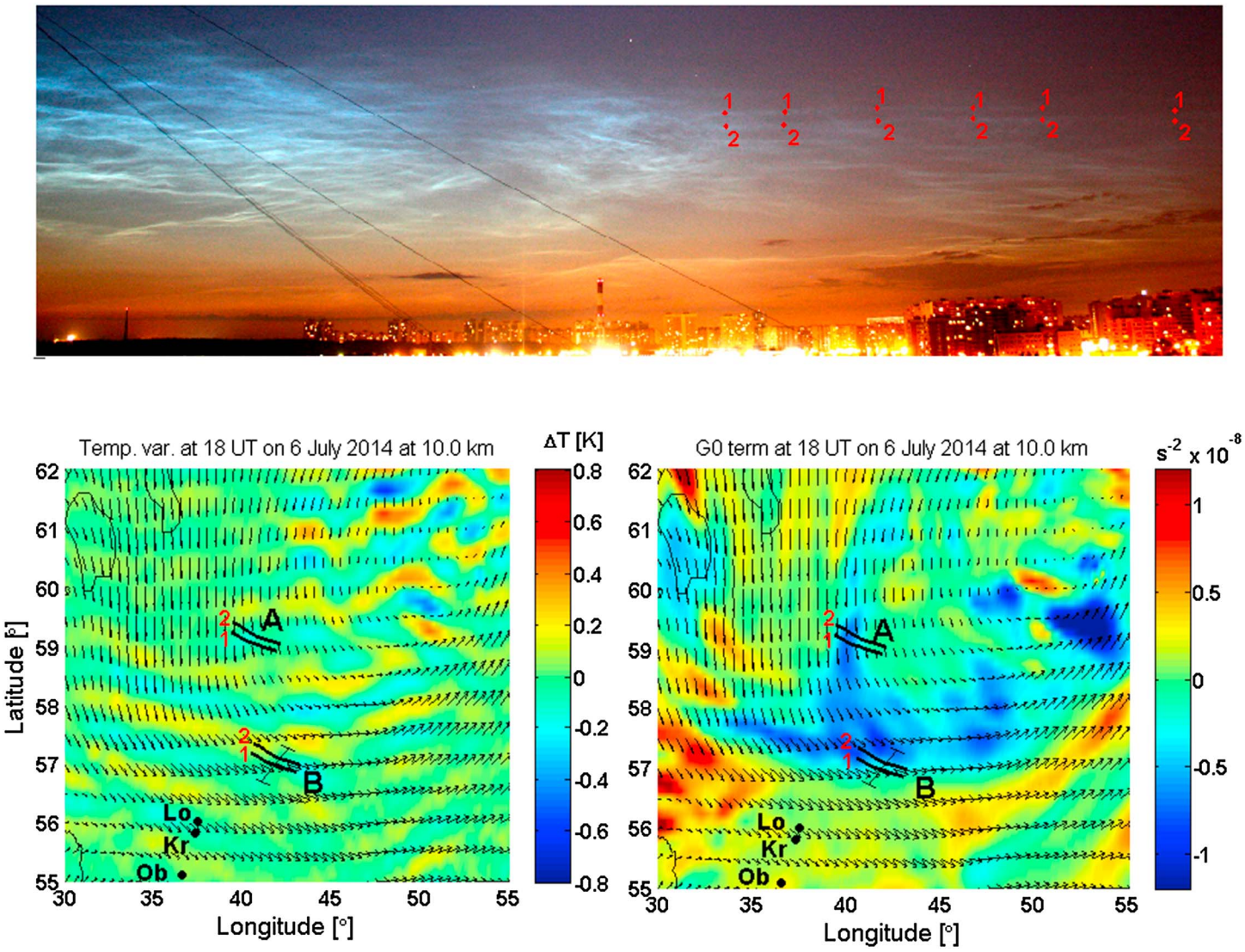

Figure 6. (top) NLC image taken from Krasnogorsk at 21:00 UT on 6 July 2014; the red dots and corresponding numbers 1 and 2 mark the two analyzed wave crests. (bottom left) Wave disturbances in the ECMWF temperature field and (bottom right) in the nonlinear wave source at 10.0 km at 18:00 UT on 6 July 2014. The other notations are the same as in Figure 5.

assumption; namely, the studied GW traveled toward the NNE and their sources were located southward and eastward of their observed positions. *Demissie et al.* [2014] have also statistically found that a significant part of GWs as observed in NLC has traveled toward the NNE over Norway. Nearly the same NE preferable direction of gravity wave propagations through the OH emission layer was found by *Stockwell and Lowe* [2001] as observed from middle-latitude stations located in southwestern Ontario. Moreover, as demonstrated in the present study, the generation source may be located significantly eastward of the meridian of the observed GW; this is due to strong westward background wind in the stratosphere and mesosphere and rather slow group velocity of the GW. Using the OI emission layer data, *Gavrilov and Shved* [1982] found the predominant directions of GW propagations coming from the southeast in the summer time. Also, *Dubietis et al.* [2011] have statistically demonstrated that there is a large asymmetry in the propagation direction of single localized GWs, with preference moving toward the NNW-NNE sector.

When comparing GW as observed in the NLC and airglow layers, one should consider the relevant difference which is outlined by *Swenson and Mende* [1994]: "One very big difference between the observations of tracers of wave structure in noctilucent clouds versus airglow is that cloud wave modulation is superimposed on an

existing cloud structure which may represent a long history of wave and other dynamic and chemical processes. Airglow emissions, on the other hand, reflect wave modulations taking place at a given time in the emission layer." Indeed, a huge NLC field with horizontal extension of about 500 km should preexist to observe a wave modulation due to propagation of very long GW crests of about the same length. Due to a complex interplay between large-scale waves (GWs, planetary waves, and tides), this happens rarely. It is common to have large interruptions in an NLC field at middle and subpolar latitudes due to processes induced by propagation of large-scale wave processes that prohibit observation of long crests of GWs with a short wavelength. Also, it is important to note that sublimation time of ice particles is much faster than their formation time [*Gadsden and Schröder*, 1989]; airglow emissions are free from this effect. At the same time, the relatively high thickness of airglow layers impose restrictions on the minimal vertical scales and horizontal phase speed of observed GW, especially at high zenith angles [e.g., *Gavrilov and Shved*, 1982].

Theoretically, a source of slowly moving GWs could be located in the troposphere due to slowly moving frontal systems [*Hines*, 1968]. However, in practice, waves slowly moving toward the northeast-south sector should be readily filtered out by the upper tropospheric jet stream flowing in a wavy west-to-east direction [*Ahrens*, 1994]. Thus, a possible source of such type of GW could occur within the jet stream at the tropopause. Indeed, on the one hand, the background westward winds in the summer stratosphere and summer mesosphere allow such a type of GW to propagate to the summer mesopause without reaching the critical level. On the other hand, geostrophic adjustment of the wind and pressure fields is known to be a significant source of the GW generation [*Obukhov*, 1949; *Fritts and Luo*, 1992; *Medvedev and Gavrilov*, 1995; *Plougonven and Zhang*, 2014], and geostrophic adjustment of the jet stream at the tropopause can generate GW propagating upward to the summer mesopause. The present study confirms this consideration.

There is a potential possibility that the observed GW could be a ducted wave, being trapped in waveguide at the mesopause and brought to the observed atmospheric volume from other sources over large horizontal distances [see, for example, *Suzuki et al*., 2013; *Xu et al*., 2015]. We have investigated this issue in the following way. The SABER data show (Figure 3) that there is the inverse temperature layer between 78 and 84 km (black solid line) that could potentially produce the thermal duct at the mesopause for the observed GW. On the right plot of Figure 3 the squared Brunt-Väisälä frequency profile is shown demonstrating regions with negative values (statically unstable layers), between which the reflection of the wave energy is possible as well. However, it is of importance that this temperature profile was instantaneously measured at 21:25 UT on 7 July 2014, meaning that this profile was not the undisturbed temperature profile but rather represented the wave-modulated profile. It implies that the observed GW could propagate under the undisturbed temperature throughout the mesopause region. Indeed, there are similar wavy oscillations with vertical wavelengths in the range of 3–5 km below (at 71–76 km) and above (at 89–99 km) the inversion layer. Another important aspect that should be kept in mind is that having the instantaneously measured temperature profile does not mean that this wave-modulated profile existed for several hours prior to the observational time to produce a more or less permanent thermal duct during the GW propagation. Our model simulation (based on undisturbed temperature profiles taken from the ECMWF and NRLMSISE-00 models) does not show any wave reflection (or evanescent wave mode) around the mesopause region (see Figure 3). Thus, we conclude that the thermal duct at the mesopause was not responsible for the observed long-wave crests seen in NLC during that night.

The SABER temperature profile in the left plot of Figure 3 reveals wavelike structures with amplitudes of 2–4 K at altitudes of 78–81 km. Amplitudes of GWs propagating from below generally increase with altitude due to the atmospheric density decrease. GWs propagating in the realistic atmosphere are subjected to dissipation and partial reflection of wave energy. Our numerical model does take account these processes. Therefore, the ratio of temperature amplitudes between 12 and 80 km altitudes increases in 25–50 times (not in ~130 times as should expect due to simplified exponential density decrease). This means that one should anticipate much smaller temperature amplitudes of propagating GWs at altitude 12.6 km than the values of 0.5–0.6 K shown in Figure 5. One should keep in mind that the wavelike perturbations shown in Figure 5 refer to longer GWs than those observed in NLC (see section 4.3.1), which could have larger amplitudes. In addition, wavelike variations shown in Figure 5 are not time filtered and contain a spectrum of GW frequencies. Due to spatial GW dispersion, wave modes of different frequencies will propagate to different regions of the upper atmosphere. Hence, only part of wavelike perturbations shown in Figure 5 would produce the observed wave structure seen NLCs. Note that the magnitudes of temperature perturbations in the upper part of midlatitude

jet stream shown in Figure 5 fairly well correspond to those obtained in previous studies measuring GW temperature disturbances in the stratosphere [e.g., *Gavrilov et al*., 2004; *Schöch et al*., 2004].

We also checked satellite images for indications of deep convection in the vicinity of the assumed region of GW generation but could not find any. Also, weather charts show no propagation of frontal systems in the given region. And since the underlying surface is free from mountains, convective, orographic, and frontal sources should be ruled out. Thus, the most likely mechanism of the GW generation could be geostrophic adjustments in the jet stream near the tropopause in the present case. Dynamical and convective instabilities and nonlinear interactions inside the upper tropospheric jet stream could generate mesoscale disturbances and produce inclinations from the geostrophic balance [see also *Gavrilov and Fukao*, 2001]. Subsequent geostrophic adjustment of wind and pressure fields may produce GW, which can propagate to the middle and upper atmosphere. Figures 5 and 6 show the existence of such mesoscale disturbances in the region of possible GW generation in the jet stream near the tropopause. Note that since the jet stream has a wavy morphology it can excite GW moving in a wide range of directions, not necessarily toward the NNE. Future studies are planned to investigate a role of the jet stream at the tropopause as a source of GWs having a broad spectrum of wave numbers and of propagation directions often seen in the NLC field.

6. Conclusions

1. Gravity waves having very long crests of 450–500 km length, with an observed period of about 32 min, but with a very short horizontal wavelength of about 20 km were registered at the summer mesopause by means of NLC images on the night of 7–8 July 2014 at three NLC stations in the Moscow region. Similar gravity wave crests have been observed on the previous night of 6–7 July, although of shorter extension of about 150 km. In both cases the wave crests were slowly moving toward the NNE against main NLC flow.
2. Ray-tracing analysis using the ECMWF data showed that the upper tropospheric jet stream of 35–45 m/s was the most likely generation source of the observed long-wave crests. A possible mechanism for the GW formation could be the nonlinear generation of GW due to geostrophic adjustment of wind and pressure fields near the tropopause.
3. We have demonstrated that there were neither critical levels nor strong dissipation between 12 km and 80 km for slowly moving GW in the space-time domain considered. This conclusion is based on the background wind profiles taken from the ECMWF and GEWM models. Thus, slow GW moving toward the NNE could readily propagate upward from the tropopause into the summer mesopause.

Acknowledgments
The work was partly supported by the Russian Scientific Foundation under contract 14-17-00685 in terms of model simulations as well as by the Russian Foundation for Basic Research under project 15-05-04975a. The authors thank the TIMED/SABER team and M.G. Mlynczak and J.M. Russell for providing the SABER temperature data. The authors are grateful to Andrey Reshetnikov and Alexander Dalin for their support in maintaining the NLC camera located in Lobnya. Users can access the data from the paper via the author: Peter Dalin (e-mail: pdalin@irf.se).

References

Ahrens, C. D. (1994), *Meteorology Today: An Introduction to Weather, Climate, and the Environment*, West Co., New York.
Andrews, D. G., J. R. Holton, and C. B. Leovy (1987), *Middle Atmosphere Dynamics*, 489 pp., Academic, New York.
Baumgarten, G., et al. (2009), The noctilucent cloud (NLC) display during the ECOMA/MASS sounding rocket flights on August 3, 2007: Morphology on global to local scales, *Ann. Geophys.*, *27*, 953–965.
Bertin, F., J. Testud, and L. Kersley (1975), Medium scale gravity waves in the ionospheric *F*-region and their possible origin in weather disturbances, *Planet. Space Sci.*, *23*(3), 493–507, doi:10.1016/0032-0633(75)90120-8.
Bidlingmayer, E. R., and A. I. Pogoreltsev (1992), Numerical model of the transformation of acoustic-gravity waves into thermal conduction and viscous waves in the thermosphere, *Izv. Russ. Acad. Sci. Atmos. Oceanic Phys. (Engl. Ed.)*, *28*(1), 48–55.
Bonavita, M. (2011), Impact and diagnosis of model error in the ECMWF Ensemble of Data Assimilations, paper presented at ECMWF Workshop on Model Uncertainty, European Centre for Medium-Range Weather Forecasts (ECMWF), U. K.
Bretherton, F. P. (1966), The propagation of groups of internal gravity waves in a shear flow, *Q. J. R. Meteorol. Soc.*, *92*(394), 466–480.
Bronshten, V. A., and N. I. Grishin (1970), *Noctilucent Clouds*, Nauka, Moscow.
Cardinali, C., N. Žagar, G. Radnoti, and R. Buizza (2014), Representing model error in ensemble data assimilation, *Nonlinear Processes Geophys.*, *21*, 971–985, doi:10.5194/npg-21-971-2014.
Chandran, A., D. W. Rusch, S. E. Palo, G. E. Thomas, and M. J. Taylor (2009), Gravity wave observations in the summertime polar mesosphere from the Cloud Imaging and Particle Size (CIPS) experiment on the AIM spacecraft, *J. Atmos. Sol. Terr. Phys.*, *71*, 392–400, doi:10.1016/j.jastp.2008.09.041.
Chandran, A., D. W. Rusch, A. W. Merkel, S. E. Palo, G. E. Thomas, M. J. Taylor, S. M. Bailey, and J. M. Russell III (2010), Polar mesospheric cloud structures observed from the cloud imaging and particle size experiment on the Aeronomy of Ice in the Mesosphere spacecraft: Atmospheric gravity waves as drivers for longitudinal variability in polar mesospheric cloud occurrence, *J. Geophys. Res.*, *115*, D13102, doi:10.1029/2009JD013185.
Cole, K. D., and M. P. Hickey (1981), Energy transfer by gravity wave dissipation, *Adv. Space Res.*, *1*, 65–75.
Dalin, P., et al. (2008), Ground-based observations of noctilucent clouds with a northern hemisphere network of automatic digital cameras, *J. Atmos. Sol. Terr. Phys.*, *70*, 1460–1472, doi:10.1016/j.jastp.2008.04.018.
Dalin, P., N. Pertsev, S. Frandsen, O. Hansen, H. Andersen, A. Dubietis, and R. Balciunas (2010), A case study of the evolution of a Kelvin-Helmholtz wave and turbulence in noctilucent clouds, *J. Atmos. Sol. Terr. Phys.*, *72*(14-15), 1129–1138, doi:10.1016/j.jastp.2010.06.011.

Dalin, P., et al. (2011), A comparison between ground-based observations of noctilucent clouds and Aura satellite data, *J. Atmos. Sol. Terr. Phys.*, *73*(14-15), 2097–2109, doi:10.1016/j.jastp.2011.01.020.
Dalin, P., et al. (2013), First common volume ground-based and space measurements of the mesospheric front in noctilucent clouds, *Geophys. Res. Lett.*, *40*, 6399–6404, doi:10.1002/2013GL058553.
Dalin, P., et al. (2015), Evidence of the formation of noctilucent clouds due to propagation of an isolated gravity wave caused by a tropospheric occluded front, *Geophys. Res. Lett.*, *42*, 2037–2046, doi:10.1002/2014GL062776.
Demissie, T. D., P. J. Espy, N. H. Kleinknecht, M. Halten, N. Kaifler, and G. Baumgarten (2014), Characteristics and sources of gravity waves observed in noctilucent cloud over Norway, *Atmos. Chem. Phys.*, *14*, 12,133–12,142, doi:10.5194/acp-14-12133-2014.
Dubietis, A., P. Dalin, R. Balciunas, and K. Cernis (2010), Observations of noctilucent clouds from Lithuania, *J. Atmos. Sol. Terr. Phys.*, *72*(14-15), 1090–1099, doi:10.1016/j.jastp.2010.07.004.
Dubietis, A., et al. (2011), Noctilucent clouds: Modern ground-based photographic observations by a digital camera network, *Appl. Opt.*, *50*(28), F72–F79, doi:10.1364/AO.50.000F72.
Eckermann, S. D., and C. J. Marks (1996), An idealized ray model of gravity wave-tidal interactions, *J. Geophys. Res.*, *101*, 21,195–21,212, doi:10.1029/96JD01660.
Eckermann, S. D., and C. J. Marks (1997), GROGRAT: A new model of the global propagation and dissipation of atmospheric gravity waves, *Adv. Space Res.*, *20*(6), 1253–1256, doi:10.1016/S0273-1177(97)00780-1.
Fiedler, J., G. Baumgarten, U. Berger, P. Hoffmann, N. Kaifler, and F.-J. Lübken (2011), NLC and the background atmosphere above ALOMAR, *Atmos. Chem. Phys.*, *11*, 5701–5717, doi:10.5194/acp-11-5701-2011.
Friedman, J. P. (1966), Propagation of internal gravity waves in a thermally stratified atmosphere, *J. Geophys. Res.*, *71*, 1033–1054, doi:10.1029/JZ071i004p01033.
Fritts, D. C., and M. J. Alexander (2003), Gravity wave dynamics and effects in the middle atmosphere, *Rev. Geophys.*, *41*(1), 1003, doi:10.1029/2001RG000106.
Fritts, D. C., and Z. Luo (1992), Gravity wave excitation by geostrophic adjustment of the jet stream. Part I: Two-dimensional forcing, *J. Atmos. Sci.*, *49*(8), 681–697.
Fritts, D. C., J. R. Isler, G. E. Thomas, and Ø. Andreassen (1993), Wave breaking signatures in noctilucent clouds, *Geophys. Res. Lett.*, *20*, 2039–2042, doi:10.1029/93GL01982.
Gadsden, M., and W. Schröder (1989), *Noctilucent Clouds*, Springer, New York.
Gavrilov, N. M., and S. Fukao (2001), Hydrodynamic tropospheric wave sources and their role in gravity wave climatology of the upper atmosphere from the MU radar observations, *J. Atmos. Sol. Terr. Phys.*, *63*, 931–943.
Gavrilov, N. M., and G. M. Shved (1982), Study of internal gravity waves in the lower thermosphere from observations of the nocturnal sky airglow [OI] 5577 Å in Ashkhabad, *Ann. Geophys.*, *38*(6), 789–803.
Gavrilov, N. M., S. Fukao, and H. Hashiguchi (1999), Multi-beam MU radar measurements of advective accelerations in the atmosphere, *Geophys. Res. Lett.*, *26*, 315–318, doi:10.1029/1998GL900279.
Gavrilov, N. M., S. Fukao, and H. Hashiguchi (2001), The MU radar study of nonlinear advective accelerations in the lower and middle atmosphere, *Phys. Chem. Earth*, *26*(C6), 429–432.
Gavrilov, N. M., N. V. Karpova, C. Jacobi, and A. N. Gavrilov (2004), Morphology of atmospheric refraction index variations at different altitudes from GPS/MET satellite observations, *J. Atmos. Sol. Terr. Phys.*, *66*, 427–435.
Gerrard, A. J., T. J. Kane, S. D. Eckermann, and J. P. Thayer (2004), Gravity waves and mesospheric clouds in the summer middle atmosphere: A comparison of lidar measurements and ray modeling of gravity waves over Sondrestrom, Greenland, *J. Geophys. Res.*, *109*, D10103, doi:10.1029/2002JD002783.
Hickey, M. P., and K. D. Cole (1988), A numerical model for gravity wave dissipation in the thermosphere, *J. Atmos. Terr. Phys.*, *50*(8), 689–697.
Hines, C. O. (1968), A possible source of waves in noctilucent clouds, *J. Atmos. Sci.*, *25*, 937–942.
Jones, W. L. (1969), Ray tracing for internal gravity waves, *J. Geophys. Res.*, *74*, 2028–2033, doi:10.1029/JB074i008p02028.
Kirkwood, S., and K. Stebel (2003), Influence of planetary waves on noctilucent clouds occurrence over NW Europe, *J. Geophys. Res.*, *108*(D8), 8440, doi:10.1029/2002JD002356.
Krassovski, V. (1972), Infrasonic variations of OH emission in the upper atmosphere, *Ann. Geophys.*, *28*, 739–746.
Marks, C. J., and S. D. Eckermann (1995), A three-dimensional nonhydrostatic ray-tracing model for gravity waves: Formulation and preliminary results for the middle atmosphere, *J. Atmos. Sci.*, *52*(11), 1959–1984, doi:10.1175/1520-0469(1995)052<1959:ATDNRT>2.0.CO;2.
Medvedev, A. S., and N. M. Gavrilov (1995), The nonlinear mechanism of gravity wave generation by meteorological motions in the atmosphere, *J. Atmos. Sol. Terr. Phys.*, *57*(11), 1221–1231.
Nakamura, T., A. Higashikawa, T. Tsuda, and Y. Matsushita (1999), Seasonal variations of gravity wave structures in OH airglow with a CCD imager at Shigaraki, *Earth Planets Space*, *51*, 897–906.
Obukhov, A. M. (1949), On the question of the geostrophic wind, *Izv. Acad. Sci. Geogr. Geophys.*, *13*, 281–306.
O'sullivan, D., and T. J. Dunkerton (1995), Generation of inertia–gravity waves in a simulated life cycle of baroclinic instability, *J. Atmos. Sci.*, *52*(21), 3695–3716, doi:10.1175/1520-0469(1995)052<3695:GOIWIA>2.0.CO;2.
Paulino, I., et al. (2016), Periodic waves in the lower thermosphere observed by OI630 nm airglow images, *Ann. Geophys.*, *34*, 293–301, doi:10.5194/angeo-34-293-2016.
Pautet, P.-D., J. Stegman, C. M. Wrasse, K. Nielsen, H. Takahashi, M. J. Taylor, K. W. Hoppel, and S. D. Eckermann (2011), Analysis of gravity waves structures visible in noctilucent cloud images, *J. Atmos. Sol. Terr. Phys.*, *73*(14-15), 2082–2090, doi:10.1016/j.jastp.2010.06.001.
Pertsev, N., P. Dalin, and V. Perminov (2015), Influence of semidiurnal and semimonthly lunar tides on the mesopause as observed in hydroxyl layer and noctilucent clouds characteristics, *Geomagn. Aeron.*, *55*(6), 811–820, doi:10.1134/S0016793215060109.
Picone, J. M., A. E. Hedin, D. P. Drob, and A. C. Aikin (2002), NRLMSISE-00 empirical model of the atmosphere: Statistical comparisons and scientific issues, *J. Geophys. Res.*, *107*(A12), 1468, doi:10.1029/2002JA009430.
Plougonven, R., and F. Zhang (2014), Internal gravity waves from atmospheric jets and fronts, *Rev. Geophys.*, *52*, 33–76, doi:10.1002/2012RG000419.
Pogoreltsev, A. I., and N. N. Pertsev (1996), The influence of background wind on the formation of the acoustic-gravity wave structure in the thermosphere, *Atmos. Oceanic Phys. (Engl. Ed.)*, *31*(6), 723–728.
Portnyagin, Y. I., and T. V. Solovjova (2000), Global empirical wind model for the upper mesosphere/lower thermosphere. I. Prevailing wind, *Ann. Geophys.*, *18*, 300–315.
Preusse, P., S. D. Eckermann, M. Ern, J. Oberheide, R. H. Picard, R. G. Roble, M. Riese, J. M. Russell, and M. G. Mlynczak (2009), Global ray tracing simulations of the SABER gravity wave climatology, *J. Geophys. Res.*, *114*, D08126, doi:10.1029/2008JD011214.

Rapp, M., F.-J. Lübken, A. Müllemann, G. Thomas, and E. Jensen (2002), Small scale temperature variations in the vicinity of NLC: Experimental and model results, *J. Geophys. Res.*, *107*(D19), 4392, doi:10.1029/2001JD001241.

Russell, J. M., III, M. G. Mlynczak, L. L. Gordley, J. Tansock, and R. Esplin (1999), An overview of the SABER experiment and preliminary calibration results, *Proc. SPIE Int. Soc. Opt. Eng.*, *3756*, 277–288.

Sato, K., S. Watanabe, Y. Kawatani, Y. Tomikawa, K. Miyazaki, and M. Takahash (2009), On the origins of mesospheric gravity waves, *Geophys. Res. Lett.*, *36*, L19801, doi:10.1029/2009GL039908.

Sato, K., S. Tateno, S. Watanabe, and Y. Kawatani (2012), Gravity wave characteristics in the southern hemisphere revealed by a high-resolution middle-atmosphere general circulation model, *J. Atmos. Sci.*, *69*(4), 1378–1396, doi:10.1175/JAS-D-11-0101.1.

Schöch, A., G. Baumgarten, D. C. Fritts, P. Hoffmann, A. Serafimovich, L. Wang, P. Dalin, A. Müllemann, and F. J. Schmidlin (2004), Gravity waves in the troposphere and stratosphere during the MaCWAVE/MIDAS summer rocket program, *Geophys. Res. Lett.*, *31*, L24S04, doi:10.1029/2004GL019837.

Stockwell, R. G., and R. P. Lowe (2001), Airglow imaging of gravity waves 1. Results from a small network of OH nightglow scanning imagers, *J. Geophys. Res.*, *106*, 17,185–17,203, doi:10.1029/2001JD900035.

Suzuki, S., K. Shiokawa, Y. Otsuka, S. Kawamura, and Y. Murayama (2013), Evidence of gravity wave ducting in the mesopause region from airglow network observations, *Geophys. Res. Lett.*, *40*, 601–605, doi:10.1029/2012GL054605.

Swenson, G. R., and S. B. Mende (1994), OH emission and gravity waves (including a breaking wave) in all-sky imagery from Bear Lake, UT, *Geophys. Res. Lett.*, *21*, 2239–2242, doi:10.1029/94GL02112.

Taylor, M. J., and M. A. Hapgood (1988), Identification of a thunderstorm as a source of short period gravity waves in the upper atmospheric nightglow emissions, *Planet. Space Sci.*, *36*(10), 975–985.

Taylor, M. J., and M. A. Hapgood (1990), On the origin of ripple-type wave structure in the OH nightglow emission, *Planet. Space Sci.*, *38*(11), 1421–1430.

Taylor, M. J., M. A. Hapgood, and P. Rothwell (1987), Observations of gravity wave propagation in the OI (557.7 nm), Na (589.2 nm) and the near infrared OH nightglow emissions, *Planet. Space Sci.*, *35*(4), 413–427.

Taylor, M. J., M. B. Bishop, and V. Taylor (1995), All-sky measurements of short period waves imaged in the OI (557.7 nm), Na (589.2 nm) and near infrared OH and O2(0,1) nightglow emissions during the ALOHA-93 campaign, *Geophys. Res. Lett.*, *22*, 2833–2836, doi:10.1029/95GL02946.

Taylor, M. J., P.-D. Pautet, Y. Zhao, C. E. Randall, J. Lumpe, S. M. Bailey, J. Carstens, K. Nielsen, J. M. Russell III, and J. Stegman (2011), High-latitude gravity wave measurements in noctilucent clouds and polar mesospheric clouds, in *Aeronomy of the Earth's Atmosphere and Ionosphere*, *IAGA Spec. Sopron Book Ser.*, vol. 2, edited by B. Hulqvist, pp. 93–105, Springer, Netherlands, doi:10.1007/978-94-007-0326-1_7.

Thurairajah, B., S. M. Bailey, D. E. Siskind, C. E. Randall, M. J. Taylor, and J. M. Russell III (2013), Case study of an ice void structure in polar mesospheric clouds, *J. Atmos. Sol. Terr. Phys.*, *104*, 224–233, doi:10.1016/j.jastp.2013.02.001.

Uccellini, L. W., and S. E. Koch (1987), The synoptic setting and possible energy sources for mesoscale wave disturbances, *Mon. Weather Rev.*, *115*(3), 721–729, doi:10.1175/1520-0493(1987)115<0721:TSSAPE>2.0.CO;2.

Untch, A., M. Hortal, and D. Salmond (2005), High-resolution experimentation at ECMWF, paper presented at High-Resolution Workshop at Yokohama, European Centre for Medium-Range Weather Forecasts (ECMWF), U. K.

Vadas, S. L., M. J. Taylor, P.-D. Pautet, P. A. Stamus, D. C. Fritts, H.-L. Liu, F. T. São Sabbas, V. T. Rampinelli, P. Batista, and H. Takahashi (2009), Convection: The likely source of the medium-scale gravity waves observed in the OH airglow layer near Brasilia, Brazil, during the SpreadFEx campaign, *Ann. Geophys.*, *27*, 231––259.

Vasil'ev, O. B., C. I. Villman, N. M. Gavrilov, V. V. Kovalenok, A. I. Lazarev, and N. P. Fast (1987), *Investigation of Noctilucent Clouds From Space*, Hydrometeoizdat Press, Leningrad, doi:10.13140/RG.2.1.1522.5444.

Witt, G. (1962), Height, structure and displacements of noctilucent clouds, *Tellus*, *14*(1), 1–18.

Xu, J., et al. (2015), Concentric gravity waves over northern China observed by an airglow imager network and satellites, *J. Geophys. Res. Atmos.*, *120*, 11,058–11,078, doi:10.1002/2015JD023786.

Yanowitch, M. (1967), Effect of viscosity on gravity waves and the upper boundary condition, *J. Fluid Mech.*, *29*(2), 209–231.

Yue, J., B. Thurairajah, L. Hoffmann, J. Alexander, A. Chandran, M. J. Taylor, J. M. Russell III, C. E. Randall, and S. M. Bailey (2014), Concentric gravity waves in polar mesospheric clouds from the Cloud Imaging and Particle Size experiment, *J. Geophys. Res. Atmos.*, *119*, 5115–5127, doi:10.1002/2013JD021385.

Zhang, F. Q. (2004), Generation of mesoscale gravity waves in upper-tropospheric jet-front systems, *J. Atmos. Sci.*, *61*(4), 440–457, doi:10.1175/1520-0469(2004)061<0440:Gomgwi>2.0.Co;2.